Article

Mechanically Robust and Thermally Conductive Nano-Porous Anodic Aluminum Oxide Templates via Thermal Stress Minimization and Alpha Phase Transformation for Interposer

Jae-Ho Yi, Ji Young Park,* Haishan Shen, and Yong-Ho Choa*

Cite This: *ACS Appl. Nano Mater.* 2023, 6, 10967−10976

Read Online

ACCESS | Metrics & More | Article Recommendations | SI Supporting Information

ABSTRACT: In the semiconductor industry, economical high-end interposer technologies with high thermal conductivity are in high demand. The recently reported anodic aluminum oxide (AAO) template has limitations of low mechanical strength and thermal conductivity due to the amorphous phase. In addition, AAO has microthickness and nanopores, and it is easy to break. In this study, the AAO template does not develop a microcrack at high temperature by controlling the pores on the front and back side of the same pore of the AAO, as concluded in the COMSOL simulation. The nonmicrocrack alpha-AAO template is mechanically robust with high thermal conductivity owing to thermal stress minimization and phase transformation (anodizing temperature and annealing treatment). In addition, anionic contamination components present on the surface of the alpha-AAO pores were removed by increasing the temperature, and the properties were investigated. The hardness and thermal conductivity of the alpha-AAO template (8.98 GPa and 13.7 W/(m·K)) were 3.3 and 6.7 times higher than those of bare-AAO (2.74 GPa and 2.08 W/(m·K)), respectively. Especially, the superior thermal conductivity of alpha-AAO was confirmed by a thermal imaging camera (TIC). The alpha-AAO template with enhanced hardness and thermal conductivity can potentially be used in various applications, such as semiconductor interposer materials and 6G wireless communication components.

KEYWORDS: anodic aluminum oxide, nanopore, hardness, thermal conductivity, alpha phase, annealing
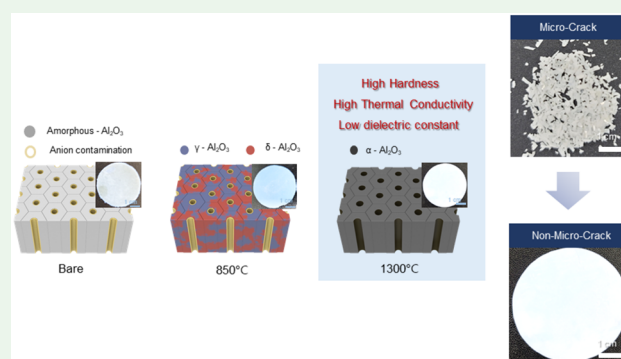
1. INTRODUCTION

Advanced interposer technology is crucial for developing highly integrated devices in packages for various applications, including custom electronics, the Internet of things, and sensors in smart factories. Interposer technology has evolved from multichip modules to Si and glass interposers; this evolution aims to simplify the manufacturing process, integrate different technologies into the interposer from vendors, and eventually decrease the overall cost.[1] Silicon and glass interposers are characterized by several well-known limitations. For example, the high electrical loss of silicon is attributed to its conductive property, overall process complexity, and cost; in contrast, high-density vias with small via diameter cannot be easily drilled using glass interposers, particularly when the glass thickness is approximately 100 μm or less, based on current drilling technologies.[2] Materials or fabrication technologies that can solve these problems are urgently required. Anodic aluminum oxide (AAO) template is electrochemically synthesized alumina with a nanoporous cylindrical structure;[3] this template is an important material in nanotechnology applications such as catalysts, gas sensors, batteries, membranes, filters, and the biological and semiconductor

industries,[4−11] owing to the convenient manufacture of the AAO template and the adjustment of pore sizes and thickness.[12] Acidic electrolytes consisting of sulfuric, oxalic, and phosphoric acid have been reported as electrolytes for synthesizing AAO templates.[13−16] The pores and thickness of the AAO template can be controlled by regulating the anodizing temperature and voltage.[17−21] Because the electrochemically synthesized AAO template contains an amorphous alumina phase, its properties, such as chemical stability, hardness, and thermal conductivity, are inferior to those of crystalline alumina.[22,23] Because of these properties, the use of the AAO templates has been limited to hard ceramic templates, owing to the AAO composition of relatively pure alumina regions and acid-contaminated regions on pore surface[24] as
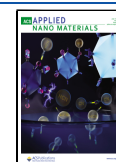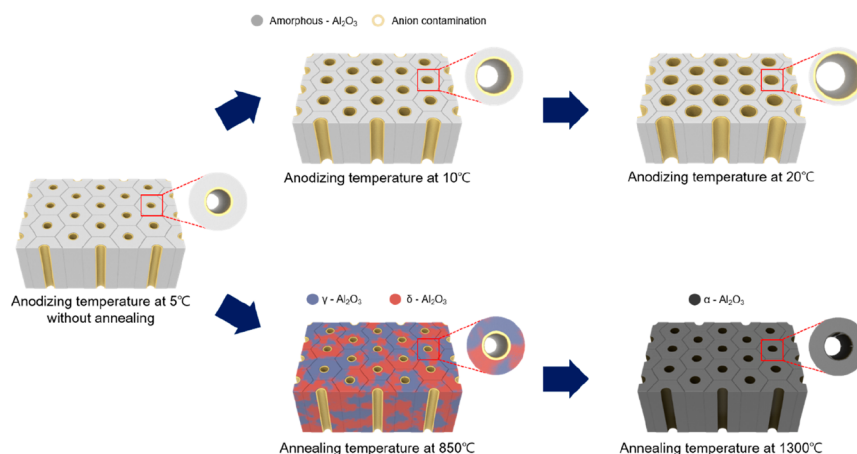
Figure 1. Fabrication mechanism for AAO templates with high hardness and thermal conductivity.

amorphous phase alumina. Nonporous thin-film type alumina exhibit Vickers hardness values of 10, 14, and 22 GPa for amorphous, gamma-, and alpha-alumina, respectively.[25] To overcome these limitations, the phase transition of amorphous AAO into a crystalline phase such as alpha-phase alumina was attempted through annealing. However, deformations such as bending and cracking occurred owing to the minute structural difference between the front and back surfaces of the AAO template.[26] To prevent these deformations, an outer layer etching process using sodium citrate was proposed. This method could prevent the deformation of the AAO templates, however, because the space of the template was predominantly empty, improving the hardness and thermal conductivity was difficult.[27]

In this study, a fabrication method and mechanism for an AAO template with high thermal conductivity and hardness were proposed. To fabricate the AAO template, oxalic acid was used as an electrolyte, and the anodization and annealing temperatures were adjusted to compare the hardness and thermal conductivity concerning the effect of the pore diameter. In addition, through COMSOL simulations, a structure wherein the AAO template did not crack despite a high heat treatment process (e.g., at 1300 °C) was determined, and these findings were applied to the experiment. The hardness, thermal conductivity, and corrosion inhibition properties of the fabricated alpha-AAO template were superior to those of a bare-AAO template.

2. EXPERIMENTAL SECTION

2.1. Materials. Oxalic acid ($C_2H_2O_4$, purity 98%), copper(II) chloride dihydrate ($CuCl_2 \cdot 2H_2O$, purity $\geq$ 99.0%), and phosphoric acid (H_3PO_4, purity $\geq$ 99.0%) were procured from Sigma-Aldrich. Ethyl alcohol anhydrous (C_2H_5OH, purity 99.9%), hydrochloric acid (HCl, assay $\geq$ 35%), and acetone (C_3H_6O, purity 99.5%) were purchased from Daejung Chemicals. Perchloric acid ($HClO_4$, assay 70.0–72.0%) was purchased from Duksan Pure Chemicals. Chromium trioxide anhydrous (CrO_3, purity $\geq$ 99.99%) was purchased from Kojundo Chemical Laboratory.

2.2. Fabrication of AAO Template Using Various Anodizing Temperatures. High-purity aluminum foil (99.999%, Alfa Aesar, USA) was cut into a rectangular shape (50 mm × 50 mm × 0.25 mm). The sheet was sonicated in anhydrous acetone for 2 min to remove organic contaminants and was subsequently electropolished in a mixed solution of perchloric acid and ethanol (1:4 volumetric ratio) at 0 °C for 120 s under an applied voltage of 20 V. To fabricate a pore, the first anodization was conducted in 0.3 M oxalic acid at 5–20

°C for 30 min at a voltage of 50 V. As a result, irregular pores were formed on the AAO surface. Subsequently, wet chemical etching was performed to remove these irregular pores. The first oxide layer produced during the first anodization step was wet-chemically removed with 1.8 wt% chromic acid and 6 wt% phosphoric acid solution at 60 °C for 2 h. Thereafter, to generate regular pores and facilitate the growth of the AAO template, a second anodization step was conducted in 0.3 M oxalic acid at 5–20 °C for 8 h at a voltage of 55 V. After anodization, the AAO/Al template was immersed in a mixture of 0.1 M copper chloride and 20 vol% HCl for 1 h to selectively remove the aluminum foil.

2.3. Fabrication of Alpha-AAO Template Using an Annealing Temperature. The effect of annealing temperature was investigated on AAO templates heat treated at bare (bare-AAO), 850 °C (gamma-delta-AAO), and 1300 °C (alpha-AAO) after anodization at 5 °C. It was also prepared at 1300 °C after anodization at 10 and 20 °C. Before removing the aluminum foil, the front surface of the AAO template was coated with stop-off lacquer (Miccrosfront, Tolber, USA) to prevent corrosion of the exposed pores in the front. In the pore-widening process, only the pores of the back surface were selectively opened. The AAO template, which was coated on the front surface, was immersed in 10 wt% phosphoric acids at 33 °C. Subsequently, the stop-off lacquer was removed using anhydrous acetone in an ultrasonication bath for 2 min. After AAO fabrication, the samples were annealed in a box furnace under an air atmosphere. Heat treatment was conducted in two steps at 850 and 1300 °C for 3 and 2 h respectively. The fabrication mechanism of the overall AAO template is depicted in Figure 1.

2.4. Characterization. The study of thermal stress was carried out with the finite element model with COMSOL Multiphysics. The three-dimensional AAO was modeled with the 75 nm pore widening, which is the same size as the upper and bottom pore size. Due to the geometry, the simulation result shows the thermal stress distribution. The morphology and pore distribution of the AAO template was characterized using a field-emission scanning electron microscope (FE-SEM, Hitachi, S-4800, Japan) after platinum sputtering for 1 min. The structures of the AAO templates were investigated concerning the front, back, and cross-sectional views to examine pore diameter and thickness. Their characteristics were measured using Image J software. All XPS spectra were collected in ultrahigh vaccum (UHV), but without exposing the sample to air, using Al Kα radiation (Thermo scientific, K-alpha, monochromatic). Emitted photoelectrons were detected with 180° double focusing hemispherical analyzer with a collimator aperture to bring the spot size at 400 μm. The vacuum pressure in the chamber ranges from 3×10^{-7} mbar to 5×10^{-8} mbar. The binding energies were calibrated against the known energy of the C–C bonding of 284.7 eV. After calibration, the spectra were corrected by subtracting a linear background. The XPS peaks were fitted with a Gaussian–Lorentzian (80% Gaussian) function requiring
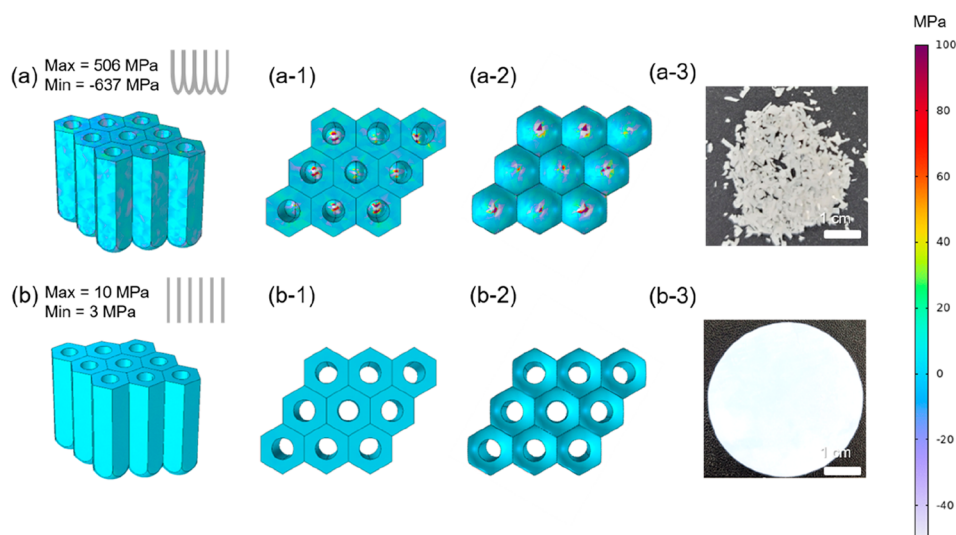
Figure 2. COMSOL simulation of (a) nonpore and (b) pore size of 75 nm (front and back); (a−b-1) front view, (a−b-2) back view, and (a−b-3) image of the real sample.

the following fitting parameters: binding energy, intensity, Lorentzian line width, Gaussian line width, and asymmetry factor.

To compare the properties according to the anodizing temperature, thermogravimetric analysis (TGA), X-Ray diffraction (XRD) patterns, Vickers hardness, dielectric constant, and thermal conductivity were examined. Thermal analysis was quantitatively conducted using TGA (Perkin-Elmer, STA 8000, USA) from room temperature to 1300 °C, and the temperature was increased at a rate of 5 °C /min. XRD patterns were analyzed to investigate the annealed AAO crystalline structure. Vickers hardness was tested using a nanoindentation tester (Fischerscope, HM2000, Germany) at a force of 2000 mN. The dielectric constant ($\mathbf{k}$) was measured using an LCR meter at 1 MHz. For moisture removal, the hot plate was set to 130 °C and AAO was placed on it to remove the absorbed water for 15 min. The mask for sputtering was manufactured by making a 1 cm × 1 cm square shape using laser cutting on the glass. Au sputtering was performed for 15 min, and each front and back surfaces of AAO were performed once. As a result of sputtering, an Au electrode with a thickness of about 90 nm was generated on the surface of AAO. After that, the copper wire and Au electrode were connected using a silver paste, and the copper wire was connected to the LCR meter using an alligator clip, as shown in Figure S1. Since the roughness of the surface measured using AFM was 6.078 nm (Figure S2), it is considered that there will be no fatal effect on the Au electrode performance of about 90 nm. The dielectric constant was calculated using the permittivity of vacuum (ε_0, 8.854 × 10^{-12} F/m) and the measured experimental capacitance (C), area (A), and thickness (D) of the gold-sputtered AAO template based on the following relation: $\mathbf{k} = C \times D/\varepsilon_0 \times A$. The thermal conductivity,[28,29] λ, was calculated as the product of density (ρ), specific heat (C_p), and thermal diffusivity (α): $\lambda = \rho \cdot C_p \cdot \alpha$

The ρ was measured using Archimedes' principle with toluene as the auxiliary liquid; C_p was measured using a differential scanning calorimeter (DSC, Shimadzu, DSC-60, Japan); α was measured using thermal wave wave analysis (ai-Phase Co. Ltd., ai-Phase Mobile M3, Japan). In addition, relative thermal conductivity was investigated using a thermal imaging camera (TIC, FLIR T620, Teledyne, Korea) for 10 min.

3. RESULTS AND DISCUSSION

3.1. Fabrication of Noncrack AAO Template Using COMSOL Simulation.
Thermal stress and tensile were simulated using COMSOL to fabricate AAO templates without nonmicro cracks. The pore diameter at the front of the template was set as 75 nm using COMSOL simulation. The

back side pore diameters were diversified to 0 and 75 nm, and the stress applied to the AAO template in the cooling process from 1300 °C to room temperature was visualized. Figure 2 shows the results of the COMSOL simulation. When the pore diameter of the back is 0, stress is concentrated in the center of the pore at the back (Figure 2a-1 to a-3). According to the simulation results, the maximum stress and tensile strength applied to the template are 506 and 637 MPa, respectively. However, when the sizes of the front and back pores are equal at 75 nm (Figure 2b-1 to b-3), the maximum stress is 10 MPa, and the maximum tensile strength applied is 3 MPa. The thermal stress of the AAO template with equal (front of 75 nm and back of 75 nm) front and back pore sizes is lower compared to not equal AAO template. Therefore, when the pore sizes at the front and back are not equal, cracks occur, and the template is broken when the AAO template is annealed at 1300 °C (Figure 2a-3). However, when the pore sizes at the front and back are equal, no cracks are generated, and thus the template is not broken (Figure 2b-3). In these simulation results, the stress applied to the AAO template is attributed to structural instability caused by the difference in pore diameter between the front and back. The fabricated AAO template has a nanoporous structure on the front and a barrier structure on the back; thus, differences are observed in the morphology and structure. The structural difference between the front and back of the AAO template causes it to crack during the annealing process. Therefore, to prevent microcracks and minimize the thermal stress on the front and back of the AAO template, identical structural characteristics are applied during fabrication.

3.2. Morphology of AAO Template.
The SEM images and pore diameters are presented in Figure S3 and Figure S4 to investigate the morphology of the AAO templates fabricated under different anodizing temperature conditions from 5 to 20 °C. The AAO templates fabricated under different temperatures have average pore diameters of 81, 96, and 103 nm on the front at 5, 10, and 20 °C, respectively, and the back has average pore diameters of 66, 73, and 94 nm, respectively. Moreover, the average porosities of the front and back surfaces are 29, 37, and 50% under the temperature conditions of 5, 10, and 20 °C, respectively. The thickness of the AAO templates is
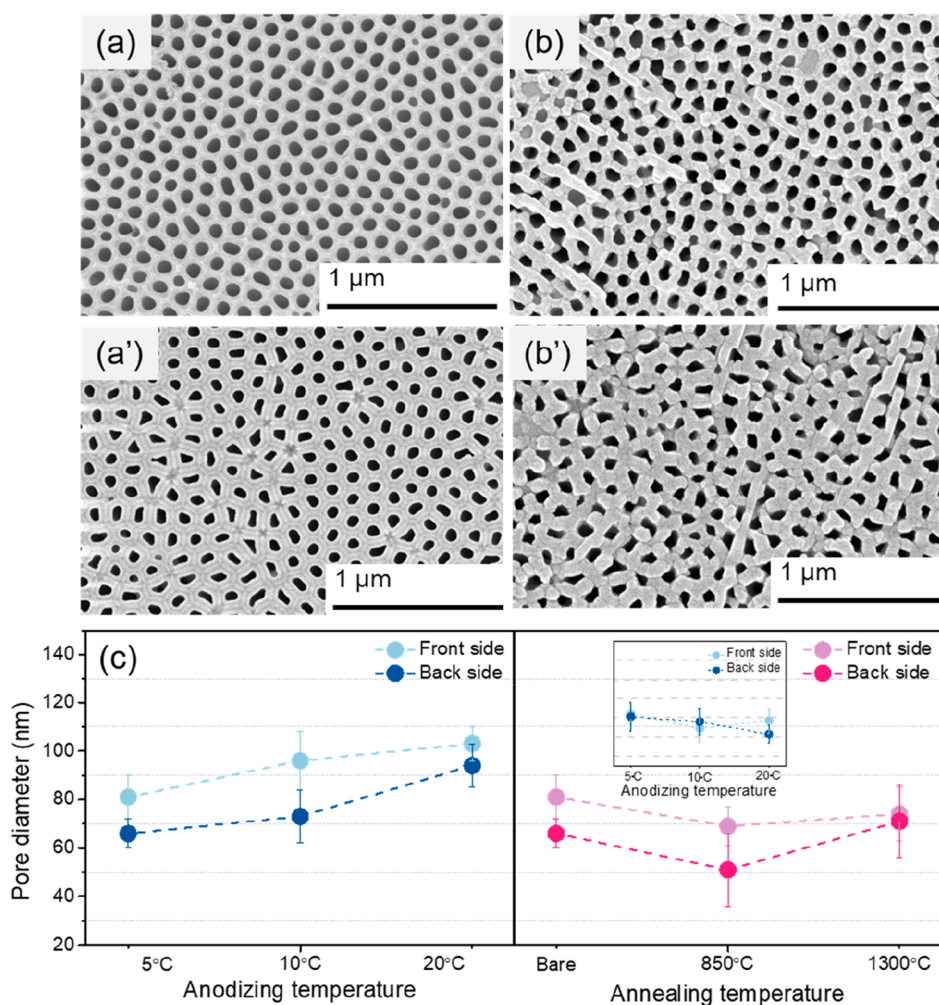
Figure 3. SEM images of (a,b) front and (a′,b′) back of the AAO template; (a,a′) anodizing temperature at 5 °C without annealing and (b,b′) annealing temperature at 1300 °C after anodizing temperature at 5 °C. (c) Summary of pore diameter; inset of annealing temperature at 1300 °C after template anodizing temperature of 5 °C, 10 and 20 °C.

increased to 92, 99, and 128 μm at anodizing temperatures of 5, 10, and 20 °C, respectively. The pore size, porosity, and thickness with different anodizing temperature are summarized in Table S1. The pore size, porosity, and thickness have the lowest values at the anodizing temperature of 5 °C (Figure 3a, a′) compared with those at 10 and 20 °C. The change in the pore diameter owing to the electrolyte temperature of the electrolyte can be explained by the enhanced field-assisted dissolution of the oxide layer. In addition, the wet-chemical etching of the acid electrolyte, according to the increase in the electrolyte temperature, widens the pore diameter.[30] The SEM images in Figure S5 present the morphology of the AAO templates fabricated under different annealing temperature conditions at 850 and 1300 °C. Bare and annealed AAO templates at 850 and 1300 °C have average pore diameters of 81, 69, and 74 nm on the front and 66, 51, and 71 nm on the back, respectively (Figure S6). Moreover, the average porosity at the front and back is 29, 25, and 27% in Table S2. As the temperature increases to 850 °C, pores of delta-gamma-AAO decrease with water of the surface and hydroxyl groups removed. Further, pores of alpha-AAO increase with the coefficient of thermal expansion increasing by increasing temperature to 1300 °C. Figure 3b, b′ demonstrates that the pore size of alpha-AAO is approximately 9 nm smaller than

that of bare-AAO. As shown in Figure 3b, b′ and c, delta-gamma-AAO and alpha-AAO are formed with smaller pore sizes than that of bare-AAO owing to thermal contraction, and alpha-AAO has a pore size difference of approximately 3 nm between the front and back in Table S2. In particular, as shown in Figure S7, all samples of the fabricated AAO template are stable without microcracks. Furthermore, as shown in Figure S8 and Figure S9, the pore size decreases due to increased thermal stress after annealing at 1300 °C upon increasing the anodizing temperature from 5 to 20 °C (Table S3).

3.3. Thermal Decomposition Behavior of AAO Template through Alpha Phase Transformation. In the anodizing reaction, Al metal is changed to Al^{3+} anion at the metal−oxide interface. Oxalic acid $(C_2H_2O_4)$ is converted to oxalate ion $(C_2O_4^{2-})$ by the applied current. Subsequently, the anions are moved to the positively charged electrode via the electric field. At this stage, light anions such as O^{2-} move rapidly and combine with Al^{3+} ions to create an inner layer composed of considerably pure Al_2O_3, and relatively heavy oxalate ions penetrate the outer layer to create a contamination layer.[24] A thermal behavior analysis method was used to investigate the decomposition mechanism of anion contamination generated during anodization. The results of TGA analysis are shown in Figure 4a. TGA of AAO is divided into
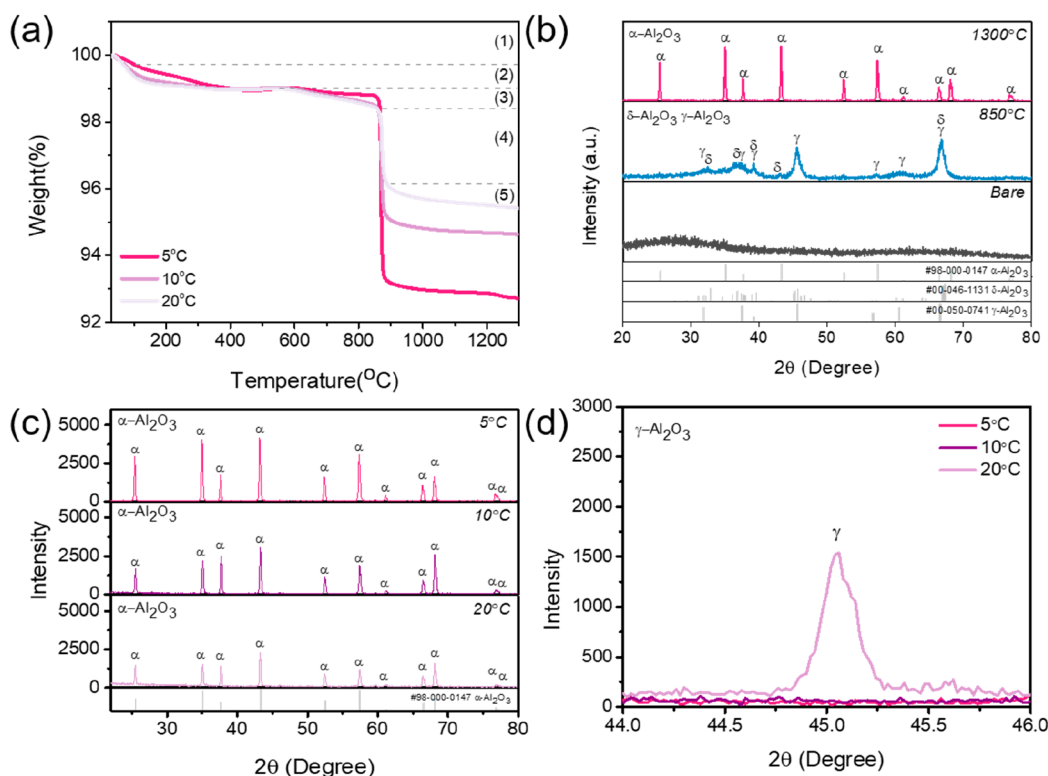
Figure 4. (a) Thermogravimetric analysis plot for the AAO template with anodizing temperatures at 5 °C, 10 and 20 °C and (b) X-ray diffraction pattern of the AAO template with annealing temperatures at 850 and 1300 °C after anodizing temperatures at 5 °C. (c) Alpha-AAO template with annealing temperatures at 1300 °C after anodizing temperatures 5 °C, 10 and 20 °C and (d) zoomed-in image from 44 to 46°.

five steps: (step 1) the moisture contained in the template evaporates up to 100 °C; (step 2) dehydration is performed to approximately 450 °C; (step 3) dehydroxylation is performed up to 850 °C; (step 4) crystallization occurs from the amorphous to the crystalline phase, and the combined oxalate ions evaporate to CO_2 gas; (step 5) finally, the gamma phase is transformed into the alpha phase when the temperature is increased from 850 to 1300 °C.[31] The TGA analysis results are used to investigate the amorphous (step 1) and crystalline structure (steps 4 and 5). XRD patterns are shown in Figure 4b. Bare-AAO exhibits an amorphous phase. The AAO annealed at 850 °C displays peaks at approximately 31.82, 37.50, 39.23, 45.63, 56.70, 60.51, and 66.56°, which can be assigned to the γ (gamma)-Al_2O_3 phase (JCPDS Card No. 00-050-0741), and at 31.84, 37.83, 39.54, and 67.29°, which can be assigned to the δ (delta)-Al_2O_3 phase (PDF No. 00-046-1131), thus indicating gamma-delta-Al_2O_3 phases. The α (alpha)-Al_2O_3 phase peaks are confirmed at approximately 25.5, 35.51, 37.70, 43.28, 52.48, 57.43, 66.45, and 68.14°, which can be assigned to the α-Al_2O_3 phase (JCPDS Card No. 98-000-0147) in AAO annealed at 1300 °C. In addition, the XRD pattern after annealing at 1300 °C is shown in Figure 4c, for which the anodizing temperature is increased from 5 to 20 °C. Consequently, the intensity of alpha-Al_2O_3 crystallinity decreases after annealing. Because the gamma-Al_2O_3 phase remains at an anodizing temperature of 20 °C in Figure 4d, the crystallinity of the alpha-Al_2O_3 phase is low. As the anodizing temperature is increased, the area of the anion contamination layer increases; thus, the crystallinity is reduced in the alpha phase. The AAO before heat treatment is amorphous, and it is believed that the lower the anion concentration, the faster the

anion is removed, and thus the higher the crystallinity of the alpha phase. In the anodization process, impurities such as oxalate ions participate between Al−O bonds. Therefore, if impurities are decomposed during annealing above 1000 °C, vacancies may occur between Al-O during the crystallization of Al_2O_3, which causes a decrease in crystallinity.

To determine the elements and chemical components constituting the AAO templates as anion contamination, the XPS profiles are presented in Figure 5. Figure 5a shows the binding energy at different annealing temperatures; C 1s, Al 2p, and O 1s binding energies are observed, and the intensity of the binding energy of C 1s is confirmed to decrease with increasing annealing temperature. The C−C bonding at 284.7 eV and C=O bonding at 289 eV is observed in Figure 5b. For the bare-AAO templates, the binding energy peaks of C−C and C=O bonding are confirmed.[32] However, for the gamma-delta-AAO and alpha-AAO templates, $(C_2O_4^{2-})$ oxalate ions are considerably decomposed, and C=O bonding is not confirmed. Moreover, the intensity of the C−C binding energy decreases from the bare-AAO to the alpha-AAO templates. Figure 5c shows that the binding energies of Al_2O_3 and $Al(OH)_3$ are observed at 73.8 and 74.8 eV, respectively.[33] For the bare-AAO template, $Al(OH)_3$ bound to the hydroxyl group of oxalic acid and Al_2O_3 produced by anodization are confirmed. For the gamma-delta-AAO templates, the hydroxyl groups start to decompose and oxidize. Therefore, the $Al(OH)_3$ peak intensity decreases, and the Al_2O_3 peak intensity increases. For the alpha-AAO templates, all the remaining hydroxyl groups are oxidized, and only the peak of Al_2O_3 is observed. Figure 5d shows the binding energy of O 1s. The Al_2O_3, C=O, and PO_3^- are observed at 530.8, 531.6, and
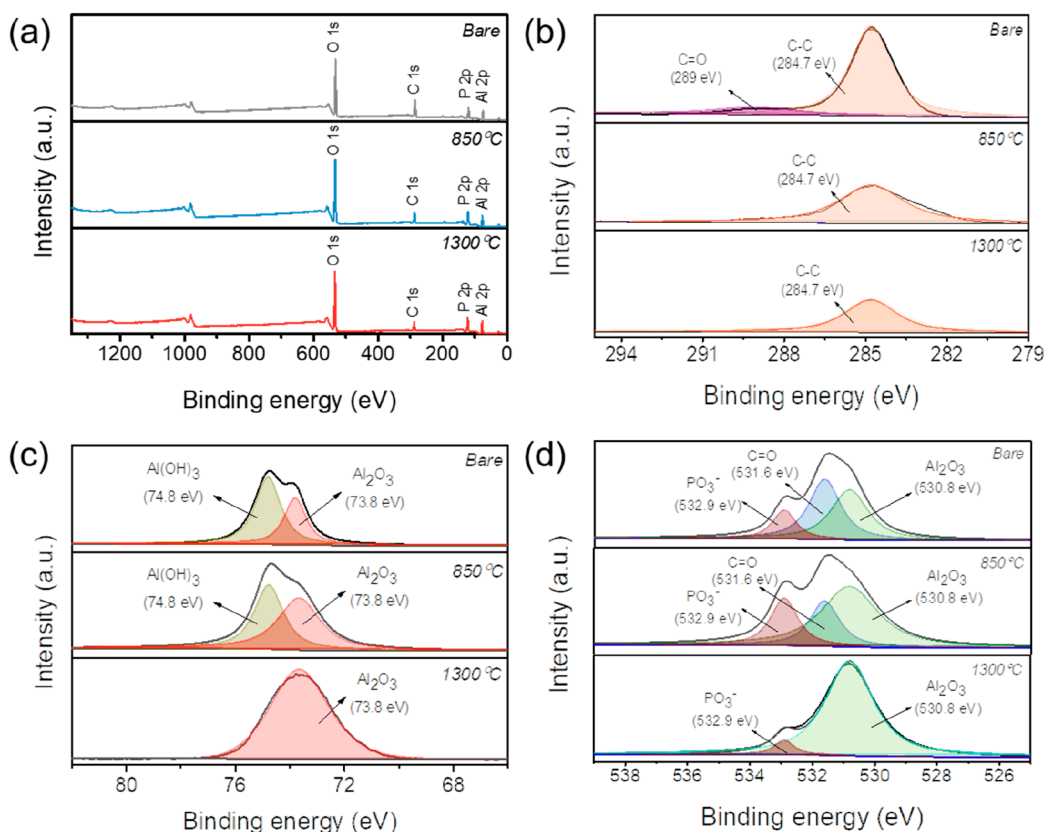
Figure 5. X-ray photoelectron spectra: (a) overall spectrum, (b) C 1s, (c) Al 2p, and (d) O 1s of AAO templates with different annealing temperatures.
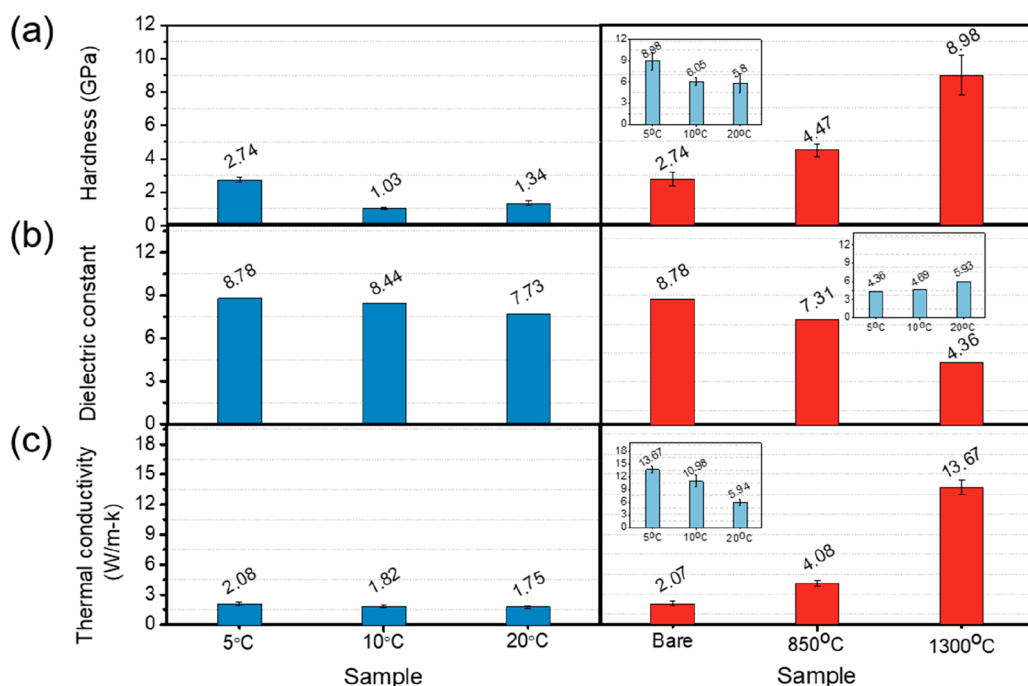

Figure 6. (a) Vickers hardness, (b) dielectric constant, and (c) thermal conductivity of AAO templates with different anodizing and annealing temperatures.

532.9 eV, respectively.[34] Al_2O_3 and C=O are produced during anodization, and PO_3^- (phosphoric) ions are produced in the pore-widening process.[35] In the alpha-AAO template, C=O

peak is not confirmed, and the fraction of Al_2O_3 is increased. An increase in the amount of Al_2O_3 and a decrease in carbon impurities through annealing are confirmed. Particularly, the

decomposition of carbon impurities and the increase in the Al_2O_3 phase according to the annealing temperature and PO_3^- ions chemically bound to the AAO template are confirmed. Similar behaviors are shown in the FT-IR spectrum in Figure S10. The Al-O peak becomes stronger, and OH^- and $C=O$ decrease as the annealing temperature increases.

3.4. High Mechanical Hardness, Low Dielectric Constant and Thermal Conductivity of Alpha-AAO Templates. Figure 6a shows the Vickers hardness according to the anodizing and annealing temperatures to confirm the mechanical hardness. Considering the anodizing temperatures, the Vickers hardness was confirmed as 2.74, 1.03, and 1.34 GPa at 5, 10, and 20 °C respectively. Especially, the annealing temperature was increased to 1300 °C, resulting in Vickers hardness was 2.74, 4.47, and 8.98 GPa for bare-AAO, gamma-delta-AAO, and alpha-AAO, respectively. Based on the different anodizing temperatures, the AAO template fabricated at 5 °C has the highest Vickers hardness. Table S1 indicates that the AAO template prepared at 5 °C has the lowest pore size of 81 (front) and 66 nm (back), and a porosity of 29%. Compared with the Vickers hardness at 10 and 20 °C, the value at the anodizing temperature of 5 °C is high, because the pore size and the porosity are the lowest. In addition, the Vickers hardness values of the alpha-AAO template are approximately 3.3 times higher than that of the bare-AAO template. This result is related to the phase transformation investigated in the XRD pattern analysis in Figure 4b because the bare-AAO, gamma-delta-AAO, and alpha-AAO templates have amorphous, gamma- and delta-Al_2O_3, and alpha-Al_2O_3 phases, respectively. Furthermore, the hardness of the AAO sample annealed at 1300 °C with anodizing temperatures of 5, 10, and 20 °C are shown in the inset of Figure 6a. These AAO templates have Vickers hardness values of 8.98, 6.05, and 5.8 GPa, respectively. When the annealing temperature is considered constant at 1300 °C, the porosity is increased by 22, 25, and 27%, respectively (Table S3). Thus, the Vickers hardness decreases with increasing anodization temperatures. Alpha-AAO was confirmed 1.5 times higher compared to the recent report of Vickers hardness of AAO in Table 1.

Table 1. Literature Survey of the Electrolyte, Pore Diameter, Porosity, and Vickers Hardness Values of AAO Templates

| Sample type	Electrolyte	Pore diameter (nm)	Porosity (%)	Vickers hardness (GPa)	Reference
Bare-AAO	Oxalic acid	81	35.35	2.74	This work
Alpha-AAO	Oxalic acid	72	28.88	8.98	
AAO	Oxalic acid	40−55	-	2.00	39
AAO	Etidronic acid	130	-	5.98	40
AAO	Phosphoric acid	-	-	1.44	41
AAO	Sulfuric acid	10	4	4.70	42

To determine the dielectric properties of the AAO templates, the dielectric constant was measured by the capacitance method at 1 MHz using an LCR meter. Figure 6b shows the dielectric constant according to the anodizing temperature at 5, 10, and 20 °C, where the samples exhibit dielectric constants of 8.78, 8.44, and 7.73, respectively. The thickness and capacitance are 92 μm and 83.8 pF, 99 μm and

75.5 pF, and 128 μm and 53.5 pF for samples prepared at 5, 10, and 20 °C, respectively. This result is related to the surface morphology of AAO templates, and the dielectric constant is found to decrease because the sample with high porosity contains several empty spaces in the template. The dielectric constant decreases with increasing annealing temperature. Bare and annealed templates at 850 and 1300 °C have dielectric constants of 8.78, 7.31, and 4.36, respectively. The thickness is 92 μm, and the capacitance is 83.8, 70.4, and 42.0 pF, respectively. The decreasing trend of the capacitance with the increasing annealing temperature can be explained using the results of TGA analysis and XPS profiles in Figure 4a and Figure 6, respectively. As capacitance refers to the ability to store an electric charge, the capacitance may vary depending on the relative amount of negative ions inside the capacitor.[36] Based on the results of TGA and XPS, anions such as carbon impurities and hydroxyl groups predominantly exist inside the bare-AAO; thus, it has a higher dielectric constant than those of the gamma-delta-AAO and alpha-AAO templates. Considering the gamma-delta-AAO template, the anion contamination is confirmed to be lower than that of bare-AAO; anions are still retained inside, and the dielectric constant is higher than that of the alpha-AAO template.[37,38] The inset data shows the dielectric constant for the template annealed at 1300 °C under the anodizing temperatures of 5, 10, and 20 °C, respectively. The capacitances of the samples fabricated at the anodizing temperatures of 5, 10, and 20 °C are 42.0, 41.9, and 41.0 pF, respectively. As the anodizing temperature is increased, the porosity increases to 23, 25, and 27%, and the thickness of the AAO template increases to 92, 99, and 128 μm, respectively, indicating that the dielectric-constant increases with increasing dielectric polarization and distance between the electrodes.

The thermal conductivity is determined depending on anodizing and annealing temperatures, as shown in Figure 6c. For the templates at 5, 10, and 20 °C, the densities are 2.874, 2.838, and 2.835 g/cm^3; the specific heats are 0.8872, 0.8501, and 0.9267 J/g·K; and the thermal diffusivities are 0.8002, 0.7524, and 0.6684 m^2/s, respectively. Each of these values is multiplied, and the thermal conductivities are calculated as 2.08, 1.82, and 1.75 W/m·K, respectively. The anodizing temperature of 5 °C results in high thermal conductivity, which is demonstrated by the AAO templates with a small pore size and low porosity. In addition, for the bare-AAO, gamma-delta-AAO, and alpha-AAO templates, the densities are 2.874, 3.267, and 3.700 g/cm^3; specific heats are 0.8872, 1.085, and 0.973 J/g·K; and thermal diffusivities are 0.8002, 1.245, and 3.792 m^2/s, respectively. The corresponding values are multiplied, and the thermal conductivities are calculated as 2.08, 4.08, and 13.67 W/m·K, respectively. In addition, alpha-AAO templates have a thermal conductivity of approximately 6.7 times higher than those of bare-AAO and gamma-delta-AAO templates. Based on the XRD patterns in Figure. 4b, the difference in thermal conductivity according to the annealing temperature is interpreted as a change in the phase transformation of AAO templates. Inset data in Figure 6c show the thermal conductivity of the templates annealed at 1300 °C, which are anodized at 5, 10, and 20 °C, respectively. The densities of the templates are 3.704, 3.827, and 3.589 g/cm^3; specific heats are 0.973, 1.125, and 1.02 J/g·K; and thermal diffusivities are 3.792, 2.643, and 1.844 m^2/s, respectively. By multiplying these values, thermal conductivities are calculated as 13.67, 10.98, and 5.945 W/m·K, respectively. These results can be

Table 2. Literature Survey of the Electrolyte, Pore Diameter, Porosity, Measurement Technique, Temperature and Thermal Conductivity Values of AAO Templates

Sample type	Electrolyte	Pore diameter (nm)	Porosity (%)	Measurement technique	Temperature (K)	Thermal conductivity	Reference
Bare-AAO	Oxalic acid	81	35.35	Temperature Wave	278	2.08	This work
Alpha-AAO	Oxalic acid	72	28.88	Temperature Wave	278	13.67	
AAO	Oxalic acid	-	-	3ω method	RT	4.82	43
AAO	Oxalic acid	35	13	Steady-state technique	RT	1.62	44
AAO	Sulfuric acid	13	8	Steady-state technique	RT	1.01	
AAO	Phosphoric acid	120	25	Laser flash	RT	1.30	45
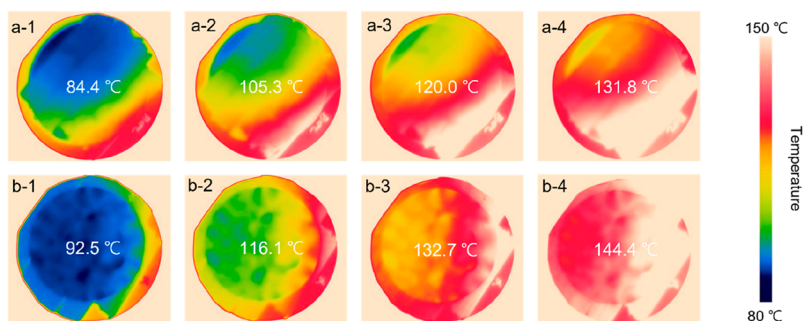
Figure 7. Thermal imaging camera (TIC) analysis of a amorphous and (b) alpha-phase AAO templates with different heating time at 150 °C heating plate, (a-b-1) 2 s, (a-b-2) 3 s, (a-b-3) 4 s and (a-b-4) 5 s after.

explained using the XRD patterns in Figure 4c and d. The AAO anodized at 5 °C shows the highest intensity and crystallinity of alpha-AAO and thus exhibits the highest thermal conductivity. The inset results show the dielectric constant for the template annealed at 1300 °C under anodization at 5, 10, and 20 °C, respectively. The capacitance of the template fabricated at 5, 10, and 20 °C anodization temperatures are 42.0, 41.9, and 41.0 pF, respectively. Furthermore, the AAO template thickness increases to 92, 99, and 128 μm, respectively. The results show that the dielectric constant decreases with decreasing dielectric polarization and increasing electrode distance. As shown in Table 2, the reported thermal conductivities of AAO templates. By controlling the type of electrolyte and anodizing temperature, the thermal conductivity for alpha-AAO is 2.8 times higher than the recently reported values.[41]

Figure 7 shows the amorphous and bare-AAO images captured using the TIC. Each sample was placed on a heating plate heated to 150 °C and the surface temperature was measured by FLIR software. Captured at the same time when the temperature started at 35 °C and increased to 150 °C. The TIC image and temperature of AAO template were shown, bare-AAO was heated to 84.4, 105.3, 120.0, and 131.8 °C, and alpha-AAO was heated to 92.5, 116.1, 132.7, and 144.4 °C. It was confirmed that the superior thermal conductive alpha-AAO was about 12 °C higher than that of amorphous AAO up to 150 °C.

4. CONCLUSION

We fabricated a hard AAO template without microcracks, and the nanopores and thickness were controlled by the anodizing temperature. The AAO template minimized thermal stress for annealing at 1300 °C owing to the equal size of the nanopores on the front and back, as determined from the COMSOL simulation. The structural change from amorphous to alpha phase confirmed that anion contamination removed impurities above 850 °C. Through structural transformation, the hardness

and thermal conductivity of the alpha-AAO template (8.98 GPa and 13.7 W/(m·K)) were 3.3 and 6.7 times higher than those of bare-AAO (2.74 GPa and 2.08 W/(m·K)), respectively. In addition, the dielectric constant decreased by approximately 2 times, from 8.78 to 4.36. The alpha-AAO template with enhanced hardness and thermal conductivity can potentially be used as an interposer material. Compared with the existing interposers, the alpha-AAO template exhibits additional degrees of freedom to manipulate material properties during fabrication, in addition to a simple manufacturing process, favorable material properties, customizable film condition, reasonable electrical performance, and low overall costs.

■ ASSOCIATED CONTENT

ⓢ Supporting Information

The Supporting Information is available free of charge at https://pubs.acs.org/doi/10.1021/acsanm.3c00396.

> Fabrication procedure; AFM measurement results; FE-SEM images; pore diameter diagrams; photographs of real AAO template samples; FT-IR spectrum; table of pore sizes, porosities, average porosity and thicknesses of AAO templates (PDF)

■ AUTHOR INFORMATION

Corresponding Authors

Ji Young Park − *Department of Materials Science and Chemical Engineering, Hanyang University, Ansan 15588, Republic of Korea*; Email: pjiyoung74@gmail.com

Yong-Ho Choa − *Department of Materials Science and Chemical Engineering, Hanyang University, Ansan 15588, Republic of Korea*; ⓞ orcid.org/0000-0002-1254-3593; Email: choa15@hanyang.ac.kr

Authors

Jae-Ho Yi − *R&D Center, Adeka Korea, Suwon 16675, Republic of Korea*

Haishan Shen − *R&D Center, NR G&C, Suwon 16681, Republic of Korea*

Complete contact information is available at:
https://pubs.acs.org/10.1021/acsanm.3c00396

Author Contributions

Notes

■ ACKNOWLEDGMENTS

■ REFERENCES

(1) Chan, H.-Y.; Zhang, Z.-H.; Bachman, M.; Li, G.-P. Porous Anodic Aluminum Oxide Interposer: Fabrication, Characterization, and Evaluation. *ECS Journal of Solid State Science and Technology* **2019**, *8* (1), P18−P23.

(2) Chan, H.-Y.; Zhang, Z.-H.; Bachman, M.; Li, G. P. Advanced Anodic Aluminum Oxide Interposer Fabrication and 3D Embedded Inductors. *2018 IEEE 68th Electronic Components and Technology Conference (ECTC)*, San Diego, CA, May 29−June 1, 2018. DOI: 10.1109/ECTC.2018.00098.

(3) Patermarakis, G.; Plytas, J. A novel theory interpreting the extremes of current during potentiostatic anodising of Al and the mechanisms of normal and abnormal growth of porous anodic alumina films. *J. Electroanal. Chem.* **2016**, *769*, 97−117.

(4) Rumiche, F.; Wang, H. H.; Hu, W. S.; Indacochea, J. E.; Wang, M. L. Anodized aluminum oxide (AAO) nanowell sensors for hydrogen detection. *Sensors and Actuators B: Chemical* **2008**, *134* (2), 869−877.

(5) Liu, X.; Sun, H.; Wu, C.; Patel, D.; Huang, J. Thermal Chemical Conversion of High-Density Polyethylene for the Production of Valuable Carbon Nanotubes Using Ni/AAO Membrane Catalyst. *Energy & Fuels* **2018**, *32* (4), 4511−4520.

(6) Ahn, Y.-k.; Park, J.; Shin, D.; Cho, S.; Park, S. Y.; Kim, H.; Piao, Y.; Yoo, J.; Kim, Y. S. Enhanced electrochemical capabilities of lithium ion batteries by structurally ideal AAO separator. *Journal of Materials Chemistry A* **2015**, *3* (20), 10715−10719.

(7) Hamouda, F.; Sahaf, H.; Held, S.; Barbillon, G.; Gogol, P.; Moyen, E.; Aassime, A.; Moreau, J.; Canva, M.; Lourtioz, J.-M.; et al. Large area nanopatterning by combined anodic aluminum oxide and soft UV−NIL technologies for applications in biology. *Microelectron. Eng.* **2011**, *88* (8), 2444−2446.

(8) Zhang, J.; Hong, G. Synthesis and photoluminescence of the Y2O3:Eu3+ phosphor nanowires in AAO template. *J. Solid State Chem.* **2004**, *177* (4−5), 1292−1296.

(9) Poostforush, M.; Azizi, H. Superior thermal conductivity of transparent polymer nanocomposites with a crystallized alumina membrane. *Express Polymer Letters* **2014**, *8* (4), 293−299.

(10) Taşaltın, N.; Öztürk, S.; Kılınç, N.; Yüzer, H.; Öztürk, Z. Z. Simple fabrication of hexagonally well-ordered AAO template on silicon substrate in two dimensions. *Appl. Phys. A: Mater. Sci. Process.* **2009**, *95* (3), 781−787.

(11) Liang, J.; Chik, H.; Yin, A.; Xu, J. Two-dimensional lateral superlattices of nanostructures: Nonlithographic formation by anodic membrane template. *J. Appl. Phys.* **2002**, *91* (4), 2544−2546.

(12) Liu, S.; Tang, S.; Zhou, H.; Fu, C.; Huang, Z.; Liu, H.; Kuang, Y. Fabrication of AAO films with controllable nanopore size by changing electrolytes and electrolytic parameters. *Journal of Solid State Electrochemistry* **2013**, *17* (7), 1931−1938.

(13) Sulka, G. D.; Stroobants, S.; Moshchalkov, V. V.; Borghs, G.; Celis, J. P. Effect of Tensile Stress on Growth of Self-Organized Nanostructures on Anodized Aluminum. *Journal of The Electrochemical Society* **2004**, *151* (5), B260.

(14) Choi, J.; Luo, Y.; Wehrspohn, R. B.; Hillebrand, R.; Schilling, J. r.; Gösele, U. Perfect two-dimensional porous alumina photonic crystals with duplex oxide layers. *J. Appl. Phys.* **2003**, *94* (8), 4757.

(15) Sulka, G. D.; Stroobants, S.; Moshchalkov, V.; Borghs, G.; Celis, J. P. Synthesis of well-ordered nanopores by anodizing aluminum foils in sulfuric acid. *J. Electrochem. Soc.* **2002**, *149* (7), D97−D103.

(16) Chu, S. Z.; Wada, K.; Inoue, S.; Todoroki, S. Fabrication and characteristics of nanostructures on glass by Al anodization and electrodeposition. *Electrochim. Acta* **2003**, *48* (20−22), 3147−3153.

(17) Stępniowski, W. J.; Bojar, Z. Synthesis of anodic aluminum oxide (AAO) at relatively high temperatures. Study of the influence of anodization conditions on the alumina structural features. *Surf. Coat. Technol.* **2011**, *206* (2−3), 265−272.

(18) Belwalkar, A.; Grasing, E.; Van Geertruyden, W.; Huang, Z.; Misiolek, W. Z. Effect of Processing Parameters on Pore Structure and Thickness of Anodic Aluminum Oxide (AAO) Tubular Membranes. *J. Membr. Sci.* **2008**, *319* (1−2), 192−198.

(19) Bai, A.; Hu, C.-C.; Yang, Y.-F.; Lin, C.-C. Pore diameter control of anodic aluminum oxide with ordered array of nanopores. *Electrochim. Acta* **2008**, *53* (5), 2258−2264.

(20) Zaraska, L.; Sulka, G. D.; Jaskuła, M. Anodic alumina membranes with defined pore diameters and thicknesses obtained by adjusting the anodizing duration and pore opening/widening time. *Journal of Solid State Electrochemistry* **2011**, *15* (11−12), 2427−2436.

(21) Lee, W.; Schwirn, K.; Steinhart, M.; Pippel, E.; Scholz, R.; Gosele, U. Structural engineering of nanoporous anodic aluminium oxide by pulse anodization of aluminium. *Nat Nanotechnol* **2008**, *3* (4), 234−239.

(22) Awad, A. M.; Shehata, O. S.; Heakal, F. E.-T. Effect of various de-anodizing techniques on the surface stability of non-colored and colored nanoporous AAO films in acidic solution. *Appl. Surf. Sci.* **2015**, *359*, 939−947.

(23) Samantilleke, A. P.; Carneiro, J. O.; Azevedo, S.; Thuy, T.; Teixeira, V. Electrochemical Anodizing, Structural and Mechanical Characterization of Nanoporous Alumina Templates. *Journal of Nano Research* **2013**, *25*, 77−89.

(24) Abbas, M. M. Electrochemical Self-Assembly of Nanoporous Alumina Templates Title. *Advances in Materials Physics and Chemistry* **2013**, *03* (05), 244−248.

(25) Edlmayr, V.; Moser, M.; Walter, C.; Mitterer, C. Thermal stability of sputtered Al2O3 coatings. *Surf. Coat. Technol.* **2010**, *204* (9−10), 1576−1581.

(26) Yi, L.; Zhiyuan, L.; Xing, H.; Yisen, L.; Yi, C. Formation and microstructures of unique nanoporous AAO films fabricated by high voltage anodization. *Journal of Materials Chemistry* **2011**, *21* (26), 9661.

(27) Chang, Y.; Ling, Z.; Liu, Y.; Hu, X.; Li, Y. A simple method for fabrication of highly ordered porous α-alumina ceramic membranes. *Journal of Materials Chemistry* **2012**, *22* (15), 7445.

(28) Morikawa, J.; Tan, J.; Hashimoto, T. Study of change in thermal diffusivity of amorphous polymers during glass transition. *Polymer* **1995**, *36*, 4439−4443.

(29) Kurihara, T.; Morikawa, J.; Hashimoto, T. Measurement of the Thermal Diffusivity of Thin Films by an AC Joule-Heating Method. *International Jounal of Termophysics* **1997**, *18*, 505−513.

(30) Zaraska, L.; Stępniowski, W. J.; Ciepiela, E.; Sulka, G. D. The effect of anodizing temperature on structural features and hexagonal arrangement of nanopores in alumina synthesized by two-step anodizing in oxalic acid. *Thin Solid Films* **2013**, *534*, 155−161.

(31) Mata-Zamora, M. E.; Saniger, J. M. Thermal evolution of porous anodic aluminas: a comparative study. *Rev Mex Fis* **2005**, *51* (5), 502−509.

(32) Cao, X.; Zhang, T.; Deng, J.; Jiang, L.; Yang, W. An extremely simple and effective strategy to tailor the surface performance of inorganic substrates by two new photochemical reactions. *ACS Appl Mater Interfaces* **2013**, *5* (3), 494−499.

(33) Yang, C.-S.; Kim, J.-S.; Choi, J.-W.; Kwon, M.-H.; Kim, Y.-J.; Choi, J.-G.; Kim, G.-T. XPS study of aluminum oxides deposited on PET thin film. *Jounral of Industrial and engineering chemistry* **2000**, *6*, 149−156.

(34) Saleema, N.; Sarkar, D. K.; Gallant, D.; Paynter, R. W.; Chen, X. G. Chemical nature of superhydrophobic aluminum alloy surfaces produced via a one-step process using fluoroalkyl-silane in a base medium. *ACS Appl Mater Interfaces* **2011**, *3* (12), 4775−4781.

(35) Chung, C. K.; Dhandapani, D.; Syu, C. J.; Liao, M. W.; Chu, B. Y.; Kuo, E. H. Role of Oxalate Anions on the Evolution of Widened Pore Diameter and Characteristics of Room-Temperature Anodic Aluminum Oxide. *Journal of The Electrochemical Society* **2017**, *164* (4), C121−C127.

(36) Hajlaoui, M. E.; Dhahri, R.; Hnainia, N.; Benchaabane, A.; Dhahri, E.; Khirouni, K. Dielectric spectroscopy study of the Ni0.2Zn0.8Fe2O4 spinel ferrite as a function of frequency and temperature. *Materials Science and Engineering: B* **2020**, *262*, 114683.

(37) Sundarabharathi, L.; Ponnamma, D.; Parangusan, H.; Chinnaswamy, M.; Al-Maadeed, M. A. A. Effect of anions on the structural, morphological and dielectric properties of hydrothermally synthesized hydroxyapatite nanoparticles. *SN Applied Sciences* **2020**, *2* (1), 94.

(38) S, L.; C, M. Structural, dielectric, cytocompatibility, and in vitro bioactivity studies of yttrium and strontium co-substituted nano-hydroxyapatite by sol−gel method. *Journal of Sol-Gel Science and Technology* **2018**, *88* (2), 296−308.

(39) Fang, T.-H.; Wang, T.; Liu, C.-H.; Ji, L.-W.; Kang, S.-H. Physical Behavior of Nanoporous Anodic Alumina Using Nano-indentation and Microhardness Tests. *Nanoscale Research Letters* **2007**, *2* (8), 410.

(40) Boonniyom, S.; Osotchan, T.; Subannajui, K. Hot embossing of anodic aluminium oxide on high-density polyethylene: a deeper understanding based on hard surface coating. *Micro & Nano Letters* **2018**, *13* (3), 357−362.

(41) Gombar, M.; Kmec, J.; Badida, M.; Sobotova, L.; Badidova, A.; Vagaska, A. Analysis of Physical Factors on Chosen Properties of Anodic Alumina Oxide (AAO) Layers and Environment. *METAL-URGIJA* **2016**, *4*, 799−802.

(42) Aerts, T.; Dimogerontakis, T.; De Graeve, I.; Fransaer, J.; Terryn, H. Influence of the anodizing temperature on the porosity and the mechanical properties of the porous anodic oxide film. *Surf. Coat. Technol.* **2007**, *201* (16−17), 7310−7317.

(43) Vera-Londono, L.; Ruiz-Clavijo, A.; Caballero-Calero, O.; Martín-González, M. Understanding the thermal conductivity variations in nanoporous anodic aluminum oxide. *Nanoscale Advances* **2020**, *2* (10), 4591−4603.

(44) Lee, J.; Kim, Y.; Jung, U.; Chung, W. Thermal conductivity of anodized aluminum oxide layer: The effect of electrolyte and temperature. *Mater. Chem. Phys.* **2013**, *141* (2−3), 680−685.

(45) Chen, C.-L.; Chen, Y.-Y.; Lin, S.-J.; Ho, J. C.; Lee, P.-C.; Chen, C.-D.; Harutyunyan, S. R. Fabrication and Characterization of Electrodeposited Bismuth Telluride films and nanowires. *J. Phys. Chem. C* **2010**, *114*, 3385−3389.